

## Real-time probe based quantitative determination of material properties at the nanoscale

This content has been downloaded from IOPscience. Please scroll down to see the full text.

2013 Nanotechnology 24 265706

(<http://iopscience.iop.org/0957-4484/24/26/265706>)

View [the table of contents for this issue](#), or go to the [journal homepage](#) for more

### Download details:

IP Address: 128.101.167.165

This content was downloaded on 06/10/2016 at 00:00

Please note that [terms and conditions apply](#).

You may also be interested in:

[Subsurface imaging of carbon nanotube networks in polymers with DC-biased multifrequency dynamic atomic force microscopy](#)

Hank T Thompson, Fabienne Barroso-Bujans, Julio Gomez Herrero et al.

[Characterization of surface stiffness and probe-sample dissipation using the bandexcitation method of atomic force microscopy: a numerical analysis](#)

Adam U Kareem and Santiago D Solares

[Mapping nanoscale elasticity and dissipation using dual frequency contact resonanceAFM](#)

A Gannepalli, D G Yablon, A H Tsou et al.

[Nanoscale mapping of contact stiffness and damping by contact resonance atomic force microscopy](#)

Gheorghe Stan, Sean W King and Robert F Cook

[Cantilever energy effects on bimodal AFM: phase and amplitude contrast of multicomponent samples](#)

Ishita Chakraborty and Dalia G Yablon

[Bi-stability of amplitude modulation AFM in air: deterministic and stochastic outcomes for imaging biomolecular systems](#)

Sergio Santos, Victor Barcons, Josep Font et al.

# Real-time probe based quantitative determination of material properties at the nanoscale

G Saraswat<sup>1</sup>, P Agarwal<sup>2</sup>, G Haugstad<sup>3</sup> and M V Salapaka<sup>1</sup>

<sup>1</sup> Department of Electrical and Computer Engineering, University of Minnesota-Twin Cities, USA

<sup>2</sup> GE Global Research, Niskayuna, NY, USA

<sup>3</sup> Characterization Facility, University of Minnesota-Twin Cities, USA

E-mail: [murtis@umn.edu](mailto:murtis@umn.edu)


Received 20 December 2012, in final form 20 December 2012

Published 4 June 2013

Online at [stacks.iop.org/Nano/24/265706](http://stacks.iop.org/Nano/24/265706)

## Abstract

Tailoring the properties of a material at the nanoscale holds the promise of achieving hitherto unparalleled specificity of the desired behavior of the material. Key to realizing this potential of tailoring materials at the nanoscale are methods for rapidly estimating physical properties of the material at the nanoscale. In this paper, we report a method for simultaneously determining the topography, stiffness and dissipative properties of materials at the nanoscale in a probe based dynamic mode operation. The method is particularly suited for investigating soft-matter such as polymers and bio-matter. We use perturbation analysis tools for mapping dissipative and stiffness properties of material into parameters of an equivalent linear time-invariant model. Parameters of the equivalent model are adaptively estimated, where, for robust estimation, a multi-frequency excitation of the probe is introduced. We demonstrate that the reported method of simultaneously determining multiple material properties can be implemented in real-time on existing probe based instruments. We further demonstrate the effectiveness of the method by investigating properties of a polymer blend in real-time.

 Online supplementary data available from [stacks.iop.org/Nano/24/265706/mmedia](http://stacks.iop.org/Nano/24/265706/mmedia)

(Some figures may appear in colour only in the online journal)

## 1. Introduction

Emergent functionality and novel properties of material can result from the physical proximity and geometric arrangement of atoms/molecules enabled by the control of matter at the atomic scale. Current needs of emerging fields, such as massive data storage and energy storage, include light weight and flexible materials with durability and stiffness that can be met with the design of material at the nanoscale. Such efforts of materials design and discovery at the atomic scale have to be accompanied by interrogation methods that have high spatial and temporal resolution to determine material properties at the nanoscale.

An important means of interrogating material at the nanoscale is based on the principles of atomic force microscopy. Ever since the invention of the probe based

method of atomic force microscopes (AFMs) by Binnig *et al* in 1986 [1], cantilever beams with a sharp tip at one end have been used to interrogate various material properties. A recent focus of probe researchers has been the quantitative imaging of material properties, particularly of properties other than topography, such as the stiffness and dissipation attributes, at the nanoscale. This focus has the potential to substantially further the impact of probe based methods on science and technology. Of particular importance is the design and interrogation of soft-matter, including polymers and bio-matter, which are increasingly being used in novel applications such as drug delivery, flexible electronics and as energy harvesting and storage material.

Among various methods of material property interrogation using probe based techniques, there is a paucity of methods for soft-matter investigation. In this paper, we report

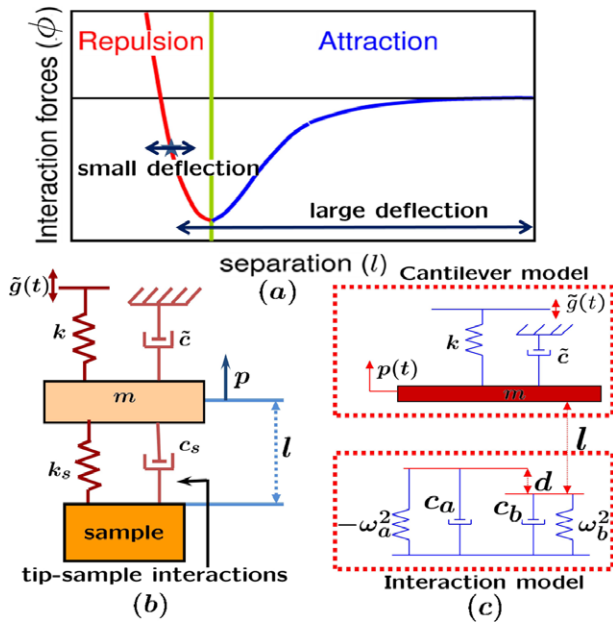


**Figure 1.** (a) Lennard Jones model for the non-linear tip-sample interaction showing tip trajectories for continuous contact (small deflections) and intermittent contact mode (large deflections). (b) Model of the cantilever-sample when deflections of the cantilever are small and non-linear interaction can be linearized. (c) Model of the cantilever-sample system with the piece-wise linear model of the non-linear cantilever-sample interaction force.

a method that simultaneously obtains estimates of the stiffness of the material and the energy lost to the sample in the *intermittent contact* mode operation of AFM, which is among the least invasive modes of probe based interrogation. The temporal resolution of the method is better than that of typical imaging speeds of AFM and, therefore, the estimates of the sample properties can be considered in real-time. Enabled by the new real-time capability of simultaneously imaging stiffness and dissipation in addition to the topography, we provide new insights into the properties of a polymer blend. This study of a polymer blend also indicates the superior lateral resolution of the imaging method, where nanometer sized domains are discernible.

Current AFM methods [2, 3] to determine material properties are predominantly *continuous contact* methods, where the cantilever is continuously interacting with the sample. In the continuous contact mode, the deflection remains small and the tip-sample interaction is either attractive or repulsive (see figure 1(a)). Under the assumption of small cantilever deflection, the sample behavior can be linearized. Here, the combined cantilever-sample system can be visualized as an equivalent spring-mass-damper (*equivalent cantilever*) with an equivalent stiffness and equivalent damping (see figure 1(b)).

Recently, a continuous contact method called band excitation (BE) was reported to determine material properties at the nanoscale. The BE method has found widespread application [4, 5]. Here, the cantilever is excited with a continuous band of frequencies near resonance, while keeping the cantilever deflection small. A second-order

model is fit to the measured response, which provides the parameters of the equivalent cantilever that represent the cantilever-sample system. The spatial resolution is dictated by the size and the distance between the pixels while the temporal resolution is limited by the large time spent at each pixel. Another recent continuous contact method [3] which offers substantial improvement in terms of bandwidth over BE uses dual AC resonance tracking (DART [6]) to estimate the equivalent parameters in the contact resonance mode of the AFM. In this method, the tip-sample contact is excited simultaneously at two frequencies on either side of the contact resonance (resonance in the case of small amplitude cantilever oscillation). These methods being contact mode are relatively harsh to the sample and are not ideally suited for soft-matter investigation. To date there are no methods that provide real-time simultaneous estimates of the dissipation and stiffness of material and are amenable to the *intermittent contact* (dynamic) mode operation of AFM [7]. The intermittent contact mode (also known as Tapping Mode<sup>TM</sup>) is a prevalent means of investigating the properties of soft-matter.

In the intermittent contact mode of AFM operation, the cantilever is oscillated with large amplitudes by a sinusoidal dither forcing at the base of the cantilever. Here the cantilever tip interacts with the sample intermittently every oscillation cycle, thus exerting extremely low lateral and frictional forces on the sample. The intermittent contact mode is gentler and less invasive, but it poses new challenges. Figure 1(a) highlights how interaction forces felt by the cantilever differ in the intermittent and continuous contact modes. In this mode, linearization of tip-sample interaction is not applicable as the tip traverses the entire non-linear interaction curve (figure 1(a)). Nevertheless, the notion of *net* attractive and *net* repulsive interaction force can be introduced. It can thus be argued that the net affect of the interaction force can either decrease (*net* attractive) or increase (*net* repulsive) the equivalent stiffness of the cantilever-sample system depending on the relative strength of attractive and repulsive forces [8]. Here, as the sample is raster-scanned in relation to the oscillatory cantilever, the amplitude and the phase of the first harmonic component (of the forcing frequency) of the cantilever trajectory are used to probe properties of the sample (see figure 2), including the topography. In existing studies, the phase of the first harmonic component of cantilever oscillation with respect to the dither forcing is heavily relied upon to gauge material properties, particularly the dissipation properties of the material. However, it is known that the phase can lead to ambiguous interpretations of the dissipation properties of material [9, 10].

Systems based principles have resulted in unparalleled results for the advancements in atomic force microscopy [11–14]. In this paper, these principles are used to develop a method for determining dissipation losses to the sample and stiffness of the material. This paper builds on the recent work by the authors (see [15]), where a method called recursive estimation of equivalent parameters (REEP) was reported. Here [15], the cantilever with a single sinusoid excitation (with large amplitude oscillation in the

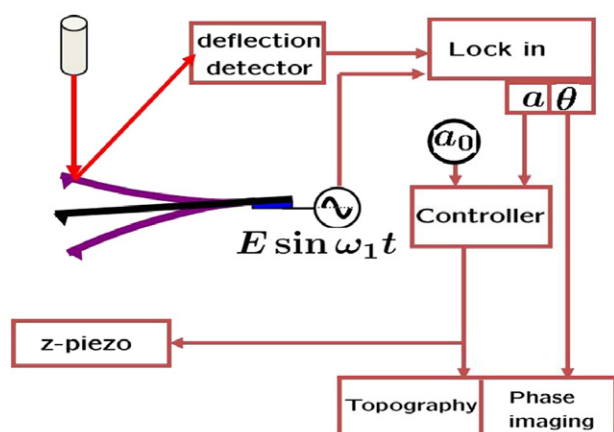


**Figure 2.** In dynamic mode AFM, the cantilever is externally excited at the first resonant frequency of the cantilever flexure. The amplitude and phase at the forcing frequency ( $a$  and  $\theta$  in the figure) are monitored to infer sample topography. A controller can be used to position the cantilever tip with respect to the sample in the  $z$  direction to regulate a set-point amplitude  $a_0$ , in which case the control signal provides the image.

range 24–200 nm) under the non-linear interaction with the sample is modeled as an equivalent cantilever (see [16, 17]). However, the equivalent cantilever parameters are estimated using a multitone excitation employing a recursive least squares method. The sensitivity of the equivalent parameters to topography was the main focus of this study. In this paper, we demonstrate that the equivalent parameter model under a multitone excitation remains valid. Toward this goal, we extend existing knowhow on averaging theory for periodically forced cantilevers, in a dynamic mode AFM operation, to a multitone excitation where the forcing is no longer periodic and thus periodic averaging theory is no longer applicable. Furthermore, we demonstrate that the estimates of the sample stiffness and dissipation can be obtained in real-time.

Before proceeding further, we note that the dissipation determined using the above methods, including the one to be presented here, cannot be taken as a direct measure of the intensive dissipation property of the material. Even if the viscoelastic dissipation properties (rate-dependent mechanical response) do not differ much between two samples, non-mechanical differences, such as molecular freedom at the surface and Hamaker constant of tip–sample interaction (which relates to the mutual polarizability of pairs of interacting atoms), can affect the total dissipation, which also contribute to adhesion hysteresis [8]. Thus probe based methods determine *total* dissipation occurring due to overall tip–sample interaction, having both bulk and interfacial sources of dissipation.

## 2. Materials and methods

### 2.1. Numerical simulation

All equations and models were simulated using custom codes in MATLAB. Standard ordinary differential equation (ODE) solvers of MATLAB were used. All the off-line data was captured through National Instrument's (NI) data acquisition card using LabView.

### 2.2. Sample

Two polymer systems were primarily used; a blend of poly(butyl methacrylate) and poly(lauryl methacrylate) (PBMA–PLMA) and a triblock copolymer of poly(styrene-block-isobutylene-block-styrene) (PS-PIB-PS or SIBS). For the PBMA–PLMA case, the solution was 15 mg ml<sup>−1</sup> of total polymers in tetrahydrofuran. The relative polymer concentration was 75:25 for PBMA–PLMA. The polymer was spin-coated onto a silicon wafer from the solution, under ambient conditions, to produce a film thickness of  $\approx 1$   $\mu$ m, followed by ambient drying. The relative polymer concentration for SIBS was 17:83 for PS:PIB with MW = 103 000. The polymer was again spun under ambient condition onto silicon wafer from 20% toluene solution, to produce a film thickness of  $\approx 1$   $\mu$ m, and dried in vacuum at 110 °C for 2 h. The SIBS film was additionally annealed overnight in the solvent vapor (small beaker of solvent under inverted larger beaker) to produce more pronounced phase segregation into cylindrical PS domains that lie predominantly parallel or perpendicular to the surface.

### 2.3. Atomic force microscopy

All experiments were performed on a commercially available AFM, MFP-3D from Asylum Research. Two Olympus cantilevers, AC240 (typical spring constant of 2 N m<sup>−1</sup> and resonant frequency of 70 kHz) and AC160 (typical spring constant of 42 N m<sup>−1</sup> and resonant frequency of 300 kHz) were used. Both cantilevers were rectangular shaped, had silicon tetrahedral tips with a typical radius of 7 nm and aluminum coating on the reflex side. For imaging, a closed loop  $x$ – $y$  nano-positioning system was used to raster scan the sample. A  $z$ -piezo was used to position the cantilever tip vertically with respect to the sample to regulate a set-point amplitude. The same  $z$ -piezo was also used to generate 'approach–retract cycle' [8] curves where the cantilever was first moved closer to the sample in the approach phase and then away from the sample in the retract phase.

## 3. Theoretical considerations

### 3.1. Arriving at the equivalent cantilever model

A first mode approximation of the cantilever dynamics results in a spring–mass–damper model of the cantilever where the sample forces are felt by the mass. For small deflections of the mass, the sample's influence can be modeled as a spring (with stiffness  $k_s$ ) and a damper (with damping  $c_s$ ), where the stiffness of the spring is given by the local slope of the curve that relates the interaction force and the cantilever–sample separation (see figure 1(b)). Here the cantilever–sample system can be envisioned to be an equivalent cantilever (another spring–mass–damper system) with changed parameters, such as the stiffness changing from  $k$  to  $k + k_s$ .

In the case where the cantilever oscillations are large, the cantilever tip explores a considerable portion of the tip–sample non-linearity, which does not allow for a linearized

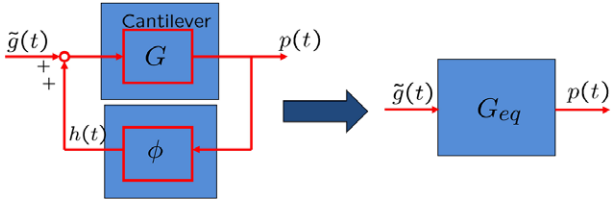


**Figure 3.** Figure showing that using averaging theory, the cantilever being forced by  $\tilde{g}(t)$  and the tip-sample separation dependent force  $\tilde{\phi}$  with the tip deflection  $p(t)$  can be viewed as an equivalent cantilever with changed resonant frequency  $f_e$  and quality factor  $Q_e$  being forced by  $\tilde{g}(t)$  resulting in the deflection  $p(t)$  (with no sample force  $\tilde{\phi}$ ).

approximation of the tip-sample interaction. However, under sinusoidal forcing it is still possible to arrive at an equivalent cantilever model of the combined cantilever-sample system by appealing to averaging theory (see figure 3 and [9]). Here, the second-order dynamics of the cantilever-sample system is given by

$$m\ddot{p} + \tilde{c}\dot{p} + kp = \tilde{\phi}(p, \dot{p}) + m\tilde{g}(t) \quad (1)$$

where  $p(t)$  is the instantaneous cantilever position,  $m$  is the mass,  $k$  is the spring constant and  $\tilde{c}$  is the damping coefficient of the first modal approximation of the cantilever;  $\tilde{g}(t)$  is the dither excitation and  $\tilde{\phi}(p, \dot{p})$  is the force due to non-linear tip-sample interaction. Let  $\omega^2 := k/m$  be the resonant frequency. Assuming that the damping  $\tilde{c}$ , forcing  $\tilde{g}$ , and the tip-sample interaction  $\tilde{\phi}$  are small, we define  $\tilde{c} = \epsilon c$ ,  $\tilde{g} = \epsilon g$  and  $\tilde{\phi} = \epsilon \phi$ , where  $\epsilon$  is a small parameter. It follows from equation (1) that

$$\ddot{p} + \omega^2 p = (\epsilon/m)\phi(p, \dot{p}) + (\epsilon/m)g(t) - (\epsilon/m)c\dot{p}. \quad (2)$$

Defining a change of coordinates from  $(p, \dot{p}) \rightarrow (a, \theta)$  via

$$p = a \cos(\omega t + \theta); \quad \dot{p} = -a\omega \sin(\omega t + \theta), \quad (3)$$

and differentiating the relations in equation (3) with respect to time, the dynamics in the changed coordinates is given by

$$\begin{aligned} \dot{a} &= -\frac{\epsilon}{\omega m} [\phi(a \cos(\omega t + \theta), -a\omega \sin(\omega t + \theta)) \\ &\quad + c(a\omega \sin(\omega t + \theta)) + g(t)] \sin(\omega t + \theta) \\ \dot{\theta} &= -\frac{\epsilon}{\omega m} [\phi(a \cos(\omega t + \theta), -a\omega \sin(\omega t + \theta)) \\ &\quad + c(a\omega \sin(\omega t + \theta)) + g(t)] \cos(\omega t + \theta). \end{aligned} \quad (4)$$

Evidently the dynamics in equation (4) is time varying and non-linear.

In the case of single frequency excitation ( $\tilde{g}(t) = E \sin \omega t$ ), the dynamics of equation (4) is periodic with period  $(2\pi/\omega)$ . Application of *first-order periodic averaging* [18] to the non-linear time varying dynamics of equation (4) results in the averaged time-invariant dynamics as described below (where with some abuse of notation the averaged amplitude and phase are also represented by  $a$  and  $\theta$ ):

$$\begin{aligned} \dot{a} &= -\frac{c_e(a)}{2m} a - \frac{\epsilon}{2m\omega} E \sin \theta, \\ \dot{\theta} &= \omega_e(a) - \omega - \frac{\epsilon}{2ma\omega} E \cos \theta, \end{aligned} \quad (5)$$

where

$$\begin{aligned} \omega_e^2(a) &= \omega^2 - \frac{2}{am} \bar{\Phi}_c, \\ \frac{c_e(a)}{2m} &= \frac{\tilde{c}}{2m} + \frac{1}{am\omega} \bar{\Phi}_d, \end{aligned} \quad (6)$$

with  $\bar{\Phi}_c = (1/2\pi) \int_0^{2\pi} \tilde{\phi}(a \cos \psi, -a\omega \sin \psi) \cos \psi d\psi$  and  $\bar{\Phi}_d = (1/2\pi) \int_0^{2\pi} \tilde{\phi}(a \cos \psi, -a\omega \sin \psi) \sin \psi d\psi$ . By reverting the averaged dynamics (equation (5)) in the  $(a, \theta)$  coordinates to the original  $(p, \dot{p})$  coordinates, the following equation can be shown to hold

$$\ddot{p} + \frac{c_e(a)}{m} \dot{p} + \omega_e(a)^2 p = \frac{1}{m} \tilde{g}(t). \quad (7)$$

The above dynamics describes an *equivalent cantilever* with changed resonant frequency  $\omega_e$  and damping  $c_e$  (depending on the slowly varying parameter  $a$ ) with no non-linear tip-sample interaction (figure 3). The equivalent stiffness is defined as  $k_e := m\omega_e^2$  and the equivalent quality factor as  $Q_e := (\sqrt{k_e m}/c_e)$ . It follows from equation (6), that the change in the stiffness and damping coefficient are given by  $-(2/a) \bar{\Phi}_c$  and  $(2/a\omega) \bar{\Phi}_d$  respectively.

To verify the *equivalent cantilever* model (equation (7)), simulations using a piece-wise linear model [17, 19] of tip-sample interaction and cantilever modeled as a second-order system with  $f_0 = 70$  kHz and  $Q = 200$  were performed. The model of the intermittent contact mode dynamics with the piece-wise linear model is described in figure 1(c). The negative spring accounts for the long-range attractive forces and the positive spring accounts for the short-range repulsive forces. The dampers account for the energy dissipation in the sample and the variable  $l$  characterizes the tip-sample separation. It can be summarized as,

$$\tilde{\phi}(p, \dot{p}) = \begin{cases} 0, & \text{if } p \geq -(l-d) \\ -\omega_a^2(p+l-d) + c_a \dot{p}, & \text{if } -l \leq p < -(l-d) \\ \omega_b^2(p+l) - \omega_a^2(p+l-d) + c_a \dot{p} + c_b \dot{p}, & \text{if } p < -l. \end{cases} \quad (8)$$

For these simulations, the *free air amplitude* (amplitude of the cantilever deflection when cantilever is not interacting with the sample) was chosen to be 24 nm, and the mean tip-sample separation ( $l$ ) was varied from 24 to 20 nm (approach phase) and back to 24 nm (retract phase) linearly with time. Such a measurement of the different aspects of the cantilever trajectory while linearly decreasing and then increasing the tip-sample separation is called a ‘force curve’ or ‘approach-retract cycle’. Figure 4 shows simulation results that provide strong corroboration that the amplitude trajectories of the averaged dynamics (equation (5)) provide a good approximation to that of the original dynamics of equation (4).

### 3.2. Deriving sample properties from equivalent cantilever parameters

It is evident that from the knowledge of the nominal parameters ( $k$ ,  $\tilde{c}$  and  $\omega$ ), the equivalent cantilever parameters



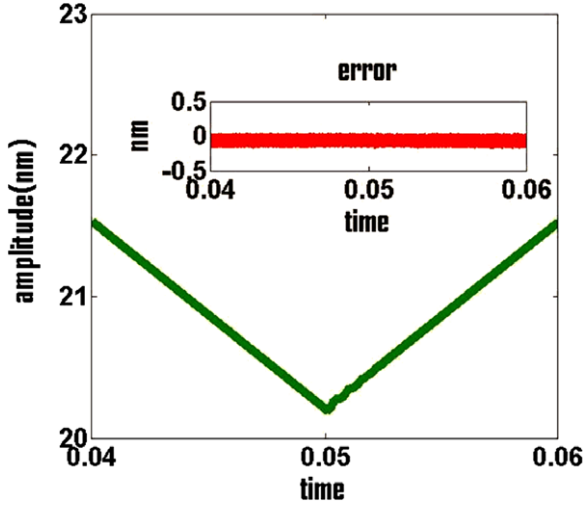


**Figure 4.** Shows the amplitude of the first harmonic. In the approach phase (from time 0.04 to 0.05) the amplitude reduces from 21.5 to 20.2 nm and in the retract phase the amplitude recovers to 21.5 nm. The amplitude as obtained by the averaged dynamics closely follows the original amplitude shown; the inset shows the error to be within  $\pm 0.1$  nm.

( $k_e$  and  $c_e$ ), and the amplitude  $a$ , it is possible to determine  $\bar{\Phi}_c$  and  $\bar{\Phi}_d$  (see equation (6)). As  $\bar{\Phi}_d$  characterizes the difference between the equivalent damping and nominal damping (where sample is absent) and  $\bar{\Phi}_c$  characterizes the difference between the equivalent resonant frequency and nominal resonant frequency (which relates to the stiffness), we can view  $\bar{\Phi}_d$  and  $\bar{\Phi}_c$  as characterizing the dissipative and conservative properties of the sample respectively. As  $\bar{\Phi}_d$  is the dissipation force per cycle,  $\bar{\Phi}_D := a\omega\bar{\Phi}_d$  is the energy dissipation per cycle. Furthermore, it can be shown that within an order  $\epsilon$

$$-\frac{1}{T} \int_0^T \phi(p, \dot{p}) \dot{p} dt = \frac{1}{T} \int_0^T (c_e - \tilde{c}) \dot{p}^2 dt = a\omega\bar{\Phi}_d \quad (9)$$

where  $-(1/T) \int_0^T \phi(p, \dot{p}) \dot{p} dt$  denotes the average power per period dissipated by the sample whereas  $(1/T) \int_0^T (c_e - \tilde{c}) \dot{p}^2 dt$  denotes the average power lost by a viscous damper in a spring-mass-damper system with damping coefficient  $(c_e - \tilde{c})$ . Thus the average power lost to the sample is equal to the average power lost by an equivalent viscous damper with coefficient  $(c_e - \tilde{c})$ , which is also equal to  $\bar{\Phi}_D$ . This further bolsters the equivalent cantilever description. It immediately follows from this discussion that if the sample is conservative then  $\bar{\Phi}_d = 0$ . A similar interpretation holds for  $\bar{\Phi}_c$  (see [20]) where the notion of reactive power in electrical circuits is generalized to mechanical systems and it can be shown that  $\bar{\Phi}_c$  represents the average reactive power.

### 3.3. Formulation of equivalent cantilever parameters estimation as system identification

To determine  $\bar{\Phi}_c$  and  $\bar{\Phi}_d$  from equation (6), it is essential to determine the equivalent resonant frequency  $\omega_e$  and damping  $c_e$ . We see that the equivalent cantilever parameters (equation (6)) depend on the slowly varying amplitude  $a$ .

It follows that if the estimation scheme is fast compared to the evolution of the amplitude dynamics, then the dynamics described by equation (7) is a linear and time-invariant system in the estimation time scale. Thus the problem of estimating equivalent cantilever parameters is transformed to identification of a linear time-invariant system (equation (7)) with the caveat that the estimation time scale should be shorter than the time scale of amplitude dynamics. In [15], the authors have reported a method (the REEP algorithm) for recursively estimating the parameters of a second-order system (equation (7)). It was observed experimentally and through simulations [15] that with mono-frequency excitation  $\tilde{g}(t) = E \sin \omega t$  it was not possible to estimate the parameters of the second-order system (equation (7)) within the desired time scale. It was concluded that multi-frequency forcing will make the estimation process more robust and faster and thus the excitation signal was chosen of the form,  $\tilde{g}(t) = \gamma \sin(\omega t) + \gamma_+ \sin(\omega + \Delta\omega)t + \gamma_- \sin(\omega - \Delta\omega)t$ . The magnitudes  $\gamma_+$  and  $\gamma_-$  and the sideband frequencies  $(\omega \pm \Delta\omega)$  are chosen to ensure that the trajectory of the cantilever is minimally altered when compared to the single frequency excitation while facilitating robustness in parameter estimation. It was shown in [15] that this is indeed possible and thus the entire operation maintains a dynamic mode behavior.

The need for  $\tilde{g}$  to be richer than a single sinusoid implies that it is difficult to have  $\tilde{g}$  to be periodic and thus *first-order periodic averaging* [18] is no longer applicable. Thus, the validity of the equivalent cantilever approximation has to be analyzed under the new excitation, which has multitones. We now analyze how much multitone excitation affects the equivalent cantilever model.

### 3.4. Multitone excitation

By using tools from [18], we derive the equivalent cantilever concept for multitone excitation. The result is summarized in the following theorem.

**Theorem 3.1.** Consider the dynamic system given by equation (2) with forcing  $\tilde{g}(t) = A \sin \gamma t + B_1 \sin(\gamma - \alpha)t + B_2 \sin(\gamma + \alpha)t$ , where  $\gamma$  is such that

$$\epsilon \Delta = \gamma^2 - \omega^2$$

with  $\alpha = \mathcal{O}(\epsilon)$ . Then the system can be approximated by that of a linear system with equivalent damping coefficient  $c_e(a)$  and equivalent resonant frequency  $\omega_e(a)$  (as in equation (7)) forced by a input of the form  $\tilde{g}(t)$  with an error of  $\mathcal{O}(\epsilon)$  on the time scale  $1/\epsilon$ .

In the derivation of the theorem, we again perform a change of coordinates via equation (3), and after some trigonometric manipulations obtain

$$\begin{pmatrix} \dot{a} \\ \dot{\theta} \end{pmatrix} = -\epsilon F(a, \theta, t, \alpha t). \quad (10)$$

Here  $F$  is a sum of finite periodic vector fields (as shown in equation (A.7)). We now introduce a new independent variable  $\tau = \alpha t$ , where the dynamics can be written as

$$\begin{pmatrix} \dot{a} \\ \dot{\theta} \end{pmatrix} = -\epsilon F(a, \theta, t, \tau) \quad (11)$$

$$\dot{\tau} = \alpha$$

with appropriate initial conditions. As it is shown in appendix that  $F$  is periodic in  $t$  over  $2\pi/\gamma$ , we can average the system over  $t$  keeping  $\tau$  constant, which gives the averaged equations

$$\begin{pmatrix} \dot{a}_{av} \\ \dot{\theta}_{av} \end{pmatrix} = -\epsilon F^0(a_{av}, \theta_{av}, t, \tau_{av}) \quad (12)$$

$$\dot{\tau}_{av} = \alpha$$

or

$$\begin{pmatrix} \dot{a}_{av} \\ \dot{\theta}_{av} \end{pmatrix} = -\epsilon F^0(a_{av}, \theta_{av}, t, \alpha t) \quad (13)$$

where  $F^0() = (\gamma/2\pi) \int_0^{2\pi/\gamma} F() dt$ .

It follows from [18] that  $a_{av}(t) - a(t) = \mathcal{O}(\epsilon)$  and  $\theta_{av}(t) - \theta(t) = \mathcal{O}(\epsilon)$  on the time scale  $1/\epsilon$ . After averaging  $F$  over the period  $2\pi/\gamma$ , and again with the approximation  $2\gamma \approx \gamma + \omega$ , we arrive at the averaged equations, given by

$$\begin{aligned} \dot{a} = & -\frac{c_e(a)a}{2m} - \frac{1}{\gamma} \left[ \frac{\cos \theta}{2} (A + (B_1 + B_2) \cos \alpha t) \right. \\ & \left. + \frac{\sin \theta \sin \alpha t}{2} (B_2 - B_1) \right] \\ \dot{\theta} = & \omega_e(a) - \omega + \frac{1}{a\gamma} \left[ \frac{\sin \theta}{2} (A + (B_1 + B_2) \cos \alpha t) \right. \\ & \left. - \frac{\cos \theta \sin \alpha t}{2} (B_2 - B_1) \right] \end{aligned} \quad (14)$$

where  $\omega_e$  and  $c_e$  are again given by equation (6). Comparing equation (14) to equation (5), the effect of multiple sine excitation is clear in terms of extra terms in the  $(a, \theta)$  dynamics. As in the case of single sinusoid excitation, by reverting the dynamics of equation (14) in the  $(a, \theta)$  coordinates to the original  $(p, \dot{p})$  coordinates, equation (7) can be recovered. This corroborates the equivalent cantilever model for multitone excitation and consequentially the validity of the REEP algorithm. Even with the multitone input, we see that the relationship between the equivalent parameters ( $\omega_e$  and  $c_e$ ) and sample properties (through  $\bar{\Phi}_d$  and  $\bar{\Phi}_c$ ) remain unchanged.

Further simulations were done to validate these result using the piece-wise linear model of equation (8). The free air amplitude was again chosen to be 24nm, and square pulses of 1 nm to the tip-sample interaction length was given as a sample. Equations (5) and (14) were solved simultaneously and the difference in trajectories determined via averaged equations; the results of a comprehensive non-linear simulation are described in figure 5. It is seen that the steady state rms error of multitone averaging equations

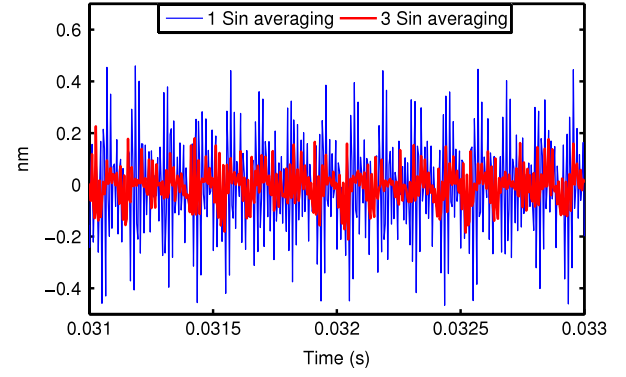


**Figure 5.** Simulation results for the difference in steady state trajectories of an actual simulation with monotone averaged equations and averaged equations with multitone excitation for a step input of 1 nm. Clearly, multitone averaging is able to better approximate the trajectories.

is less ( $\approx 60\%$  less) when compared to the mono-frequency averaging equations. A detailed derivation of the theorem 3.1 is given in supporting material.

#### 4. Recursive estimation of equivalent parameters

In the previous section, the concept of *equivalent cantilever* was corroborated for the multi-frequency excitation which is required for estimation of equivalent parameters. Now, we present the details of the REEP algorithm. A general schematic of REEP [15] setup is shown in figure 6. The cantilever is excited with a sum of three sinusoids via dither piezo. Apart from the central frequency of excitation (which is at or close to the first modal resonant frequency of the cantilever), two side frequencies are chosen to provide enough frequency content to the deflection signal ascertaining the fast convergence of recursive algorithm. Amplitudes of these side bands are set such that the orbit of the cantilever deflection does not differ much from nominal dynamic mode operation. A general discretized second-order dynamics that represents the *equivalent cantilever* can be written as,

$$\begin{aligned} e(n) &= \vartheta(n) + b_1 \vartheta(n-1) + b_0 \vartheta(n-2) \\ u(n) &= a_2 g(n) + a_1 g(n-1) + a_0 g(n-2) \\ p(n) + b_1 p(n-1) + b_0 p(n-2) &= u(n) + e(n), \end{aligned} \quad (15)$$

where  $p(n)$  and  $g(n)$  denote the cantilever deflection and dither forcing at sampled time  $t = nT_s$  where  $T_s$  is the sampling interval,  $a_i$ 's and  $b_i$ 's are respectively the numerator and denominator of the second-order discrete model of the *equivalent cantilever* and  $\vartheta(n)$  is zero mean white measurement noise with variance  $\sigma_\vartheta^2$ .

On identification of the *equivalent cantilever* (plant) at different levels of tip-sample interaction, via frequency sweep, it was observed that the coefficients  $a_2$ ,  $a_1$  and  $a_0$ , which capture the delays in the system, do not change much and contribute to the response of system at frequencies considerably away from the cantilever resonance. Subsequently the values of  $a_2$ ,  $a_1$  and  $a_0$  are fixed to the

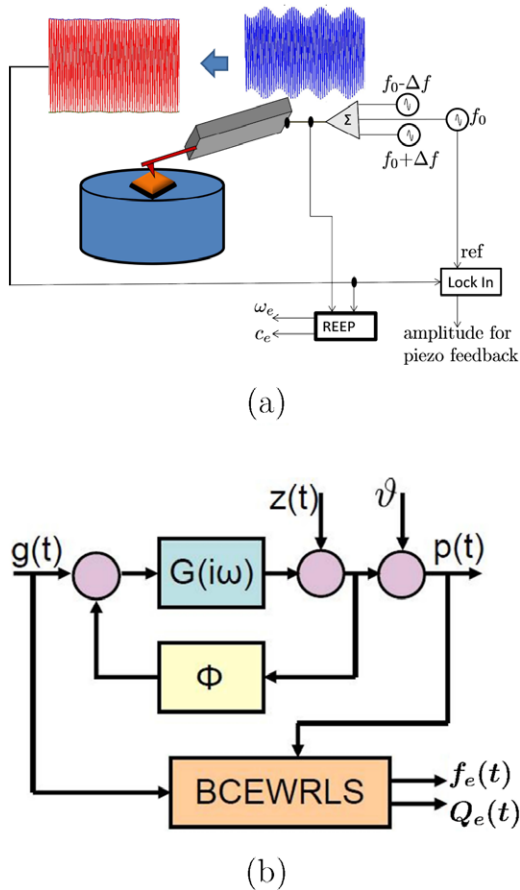


**Figure 6.** (a) Schematic of the REEP setup using a sum of three sinusoids as the drive signal to the cantilever. Two side frequencies are chosen such that the orbit of the cantilever deflection does not differ much from the tapping mode operation. (b) Modeling the cantilever-sample interaction in tapping mode operation as a  $G$ - $\Phi$  interconnection, where  $G(i\omega)$  is the second-order cantilever beam model and  $\Phi$  is the non-linear tip-sample force.  $g(t)$ ,  $z(t)$ ,  $\vartheta$  and  $p(t)$  are the dither forcing, the sample height profile, the measurement noise and measured cantilever deflection respectively. The BCEWRLS algorithm takes  $g(t)$  and  $p(t)$  as input and provides the estimates of the equivalent resonant frequency,  $f_e$ , and quality factor,  $Q_e$  (which can be used to calculate  $k_e$  and  $c_e$  directly), of the cantilever in real-time.

sample-free model values and  $b_1, b_0$  are the remaining parameters to be estimated. Equation (15) can be written as

$$z(n) = \underbrace{[b_1 \ b_0]}_{\theta} \underbrace{\begin{bmatrix} -p(n-1) \\ -p(n-2) \end{bmatrix}}_{\phi(n)} + e(n) \quad (16)$$

where  $\theta$  represents the vector of unknown parameters and  $z(n) = p(n) - a_2 g(n) - a_1 g(n-1) - a_0 g(n-2)$ . At any time instant  $t = nT_s$ , past data  $z(k)$  and  $\phi(k)$  for  $k = 0, 1, \dots, n$  are available. In [15], an estimate  $\hat{\theta}_{LS}$  of  $\theta$  was determined recursively by solving an exponentially weighted least square problem. Here  $e(n)$  is correlated and it depends on  $\vartheta(n)$ ,  $\vartheta(n-1)$  and  $\vartheta(n-2)$ , which results in the estimate  $\hat{\theta}_{LS}(n)$  converging to  $\theta$  within a bias. This generates a need to derive a suitable bias correction term for the estimation. Using the principle from a recently reported method [21] for a

bias compensated recursive least square, a bias compensated exponentially weighted recursive least squares (BCEWRLS) method was developed, as a handle on the convergence rate of the parameter estimates is also required. Derivation of the entire algorithm is included in a manuscript in preparation, which is attached, for submission to IEEE Transactions on Circuits and Systems.

#### 4.1. Verification of the REEP estimates

To verify the convergence of REEP estimates to the actual equivalent parameters, simulations were performed using the piece-wise linear model (equation (8)) of tip-sample interaction. In the simulation environment, we have access to the non-linear forcing, the instantaneous amplitude, and cantilever's natural parameters, which can be used to calculate the equivalent parameters at different tip-sample separation from equation (6). Since REEP and averaging theory are two separate methods to find the equivalent parameters, their comparison can be used to validate both or either of the two theories.

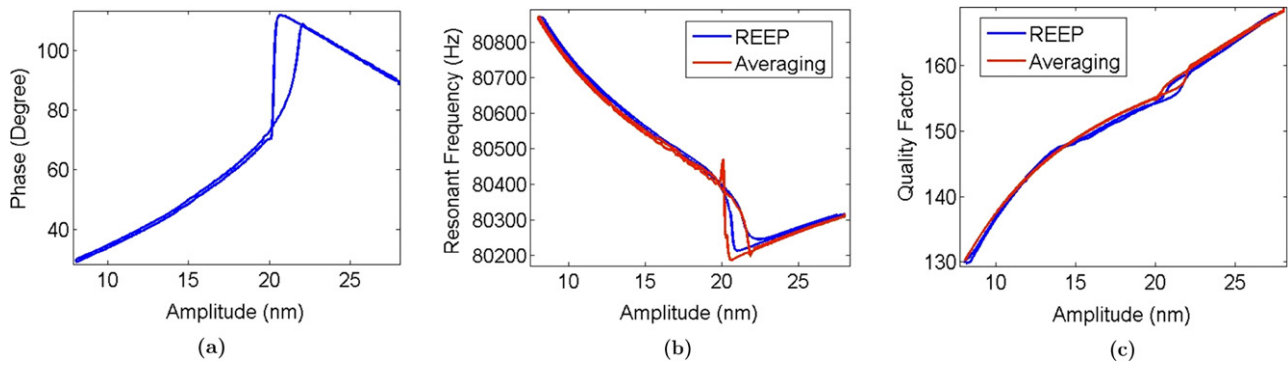
For simulations, the off-sample cantilever model was assumed to have a resonant frequency of 80.318 kHz, a quality factor of 168 and a free air amplitude of 28 nm. For the results provided here, non-linear tip-sample force parameters were chosen such that interaction was predominantly repulsive. Tip-sample separation was reduced from 28 nm to 8 nm and then increased back to 28 nm in the approach-retract cycle.

Figure 7 shows the phase, estimated resonant frequency and estimated quality factor versus amplitude in the approach-retract cycle performed. As the tip-sample interaction force changes from net attractive to significantly net repulsive, a sudden jump in the cantilever model between stable branches of the net attractive and net repulsive occurs, which is visible in figure 7. The blue curve estimates are obtained using the REEP algorithm and the red curve estimates are obtained analytically using the equations of averaging theory. It can be seen from these plots that the two independent equivalent resonant frequency and quality factor estimates match quantitatively. The slight deviation between the two estimates at low set points of amplitude is most likely because the averaging theory is valid under gentle interactions that might not hold at low setpoints. Simulations were also done for the two cases when the interaction is predominantly attractive and when the interaction is neither predominantly attractive nor repulsive. They showed similar agreement as well, as seen from figures B1 and B2 (provided in supporting information available at [stacks.iop.org/Nano/24/265706/mmedia](http://stacks.iop.org/Nano/24/265706/mmedia)).

#### 4.2. Off-line experimental results

Here a silicon cantilever, AC240TS, from Olympus with resonance frequency 78.837 kHz and spring constant  $2 \text{ N m}^{-1}$  (calculated using equi-partition method after taking a thermal response) was used to evaluate the efficacy of the method. Experiments were performed on different polymer samples and the dither and deflection signals were sampled at





**Figure 7.** Figure shows (a) phase (b) equivalent resonant frequency and (c) equivalent quality factor of the cantilever versus amplitude curves during the approach–retract cycle of the tip–sample separation. The phase plot indicates that the tip–sample interaction is net attractive at low interaction levels while it is net repulsive at higher interaction levels during the approach–retract cycle. The cantilever amplitude also jumps from the stable attractive branch to the stable repulsive branch and vice-versa during the force curve. This behavior is consistent in all the three figures. The jump locations and magnitudes are also captured in both the algorithms. Red plots are obtained from averaging theory while the blue plots are obtained from the REEP algorithm.

500 kHz simultaneously. The sampled data was used to obtain estimates of  $k_e$  and  $c_e$  off-line on MATLAB. Equation (6) was used to calculate  $\tilde{\Phi}_d$  and  $\tilde{\Phi}_c$ . The sampled deflection signal was demodulated in MATLAB and the instantaneous amplitude was used to determine  $\tilde{\Phi}_D$ . Figure 8(a) plots  $\tilde{\Phi}_D$  versus amplitude during an approach–retract cycle for two different polymers, PBMA and PLMA. It shows the agreement between the power dissipated as estimated by REEP and via analytical means [22] for experimental data obtained for both polymers. The data confirms that the REEP method does indeed provide good estimates of the power dissipated.

The real utility of the REEP algorithm is the *simultaneous* determination of the *local stiffness* of the sample and the *local dissipation*, which is evident in the  $\tilde{\Phi}_c$  and  $\tilde{\Phi}_d$  images of a SIBS (see section 2) block copolymer (see figures 8(c) and (d)), where the data was collected off-line and the equivalent parameters estimated off-line.  $\tilde{\Phi}_c$  and  $\tilde{\Phi}_d$  were determined from the equivalent parameters. The net power dissipated due to interaction with the sample depends on the extent of the sample deformation caused by the intermittent contact with the tip; more compliant samples will lead to large deformation whereas stiffer samples will lead to smaller deformation. Thus the contrast in the phase image is a combination of the intensive dissipativity and the compliance of the material. The experimental data in figure 8 indicates that the contrast in the phase image is caused by the different stiffness of styrene and isobutylene and less likely due to changes in intensive dissipative properties. These results indicate that simultaneous determination of local stiffness and damping will enable new capabilities toward understanding material properties. It is to be noted that this is the first time both dissipative as well as conservative power (also, the local stiffness and local damping coefficient) are being obtained in a dynamic mode investigation.

As mentioned earlier, the rate of convergence of estimates of the equivalent parameters is faster than the rate of evolution of amplitude dynamics, this facilitates real-time estimation of these properties. Real-time implementation of the algorithm on a hardware module is presented next.

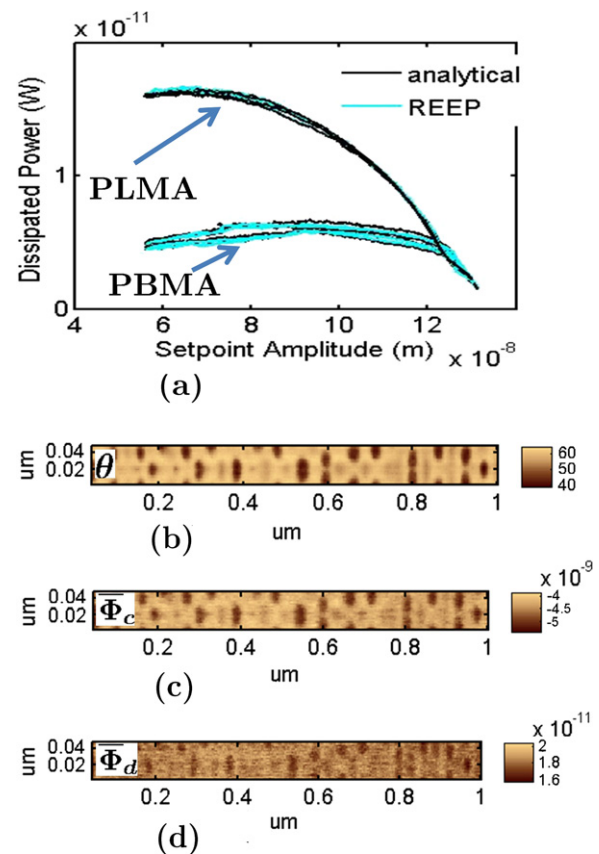


**Figure 8.** (Experimental data; off-line) (a) Comparison of power dissipated as determined by  $\tilde{\Phi}_D$  from REEP and via an analytical method described in [22] for two polymers PLMA and PBMA at two different locations for each polymer. It is known that PBMA is less dissipative than PLMA, as confirmed with the results shown. (b) the phase image (c)  $\tilde{\Phi}_c$  image (d)  $\tilde{\Phi}_d$  image of a SIBS block copolymer. The image size is  $\approx 0.05 \mu \times 1 \mu$ , stretched in y-axis by a factor of 2 to increase clarity. Note the high contrast that differentiates the domains of styrene (about 10 nm in width) on isobutylene is high in the phase image. The contrast in the  $\tilde{\Phi}_c$  image that characterizes the conservative (reactive) power is high; however, the contrast is minimal in the dissipative power characterized by  $\tilde{\Phi}_d$ . Thus isobutylene and styrene have similar dissipative characteristics but different stiffness.

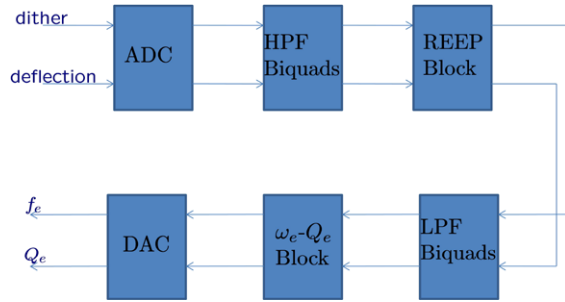


Figure 9. Block diagram of the real-time hardware module.

## 5. Real-time implementation

Over the course of multiple experiments, cantilever dynamics change and often the cantilever has to be changed. It is desirable to have the ability of changing the module parameters in an easy fashion to incorporate any change in the cantilever dynamics. The FPGA based solution offers reconfigurable hardware which facilitates design reuse and a high-bandwidth implementation. The design parameters can be changed easily. Xilinx Virtex 2-Pro30 board from Avnet Inc. was used to implement the algorithm.

### 5.1. Individual blocks

Figure 9 provides a schematic of various blocks of the module which were synthesized. A brief description of each block is given below.

- REEP Block: This is the main block running the recursive algorithm.
- Biquad Filters: For input conditioning, two high-pass filters were needed. Mostly to remove any drift and/or DC bias in the inputs (deflection signal and dither forcing). Two low-pass filters to remove high-frequency content of estimated  $b_0$  and  $b_1$  were also needed. Total of 4 biquad filters (based on Sallen-key architecture) were implemented.
- $\omega_e - Q_e$  block: This block implements equation of converting discrete parameters,  $b_0$  and  $b_1$ , to continuous time estimates of equivalent resonant frequency  $\omega_e$  and equivalent quality factor  $Q_e$ .
- ADC and DAC blocks: Analog-to-Digital Converters (ADC) and Digital-to-Analog Converters (DAC) were used to interface Digital Hardware with Analog signals of AFM.

Due to the need for high precision, algorithm was implemented in floating point representation using the open source floating point library FPLibrary-v0.94. In section 6, we document testing of the module while imaging PBMA–PLMA polymer blend with MFP-3D.

## 6. Experiments and results

Experiments were performed on PBMA–PLMA polymer blend. An Olympus cantilever (AC160TS) with resonance

frequency 334.7 kHz, spring constant 36 N m<sup>-1</sup> (determined using the thermal response of the cantilever) and quality factor of 491 was used on a MFP-3D, AFM. The FPGA module with a closed-loop bandwidth of 1.5 MHz was able to estimate the parameters of the equivalent cantilever accurately. Figures 10(a) and (b) show a comparison of the parameters as estimated off-line using MATLAB and as estimated by the FPGA based real-time module. The results show a good match on the estimation of the equivalent resonant frequency  $f_e (= \omega_e/2\pi)$  and equivalent quality factor  $Q_e$  determined while performing an approach–retract cycle on the PLMA polymer. Here, the dither excitation signal consisting a sum of three sinusoids was generated externally and fed to both the AFM and the FPGA. The deflection signal from AFM was buffered and supplied to the FPGA.

For imaging purposes, internal data acquisition channels of MFP-3D were used to save the two estimated parameters along with height, amplitude and phase image. Once the imaging was done,  $\bar{\Phi}_c$  and  $\bar{\Phi}_d$  images were directly obtained from  $f_e$ ,  $Q_e$  and amplitude images using simple arithmetic of equation (6). Figure 10 further illustrates the results of a 20  $\mu\text{m} \times 20 \mu\text{m}$  scan of a PBMA–PLMA polymer blend, where Figures 10(c)–(f) show images of  $f_e$ ,  $Q_e$ ,  $\bar{\Phi}_c$  ( $-\bar{\Phi}_c$  was plotted as the conservative force is negative) and  $\bar{\Phi}_d$  respectively. Similar to the observations in [23], three different types of domains are observed. The small circular domains approximately 200 nm in diameter are formed by the polymer PBMA. The intermediate circular domains (with diameter  $\approx 500$  nm) and the large circular domains (with diameter in the range 1–4  $\mu\text{m}$ ) are formed by the polymer PLMA.

For the three polymer domains, an estimate of the average stiffness and dissipation values was determined from the  $\bar{\Phi}_c$  and  $\bar{\Phi}_d$  values at ten different locations of each domain. Figures 11(a) and (b) plots the mean together with the standard deviation of  $\bar{\Phi}_c$  and  $\bar{\Phi}_d$  respectively for each of the three domains. Both types of PLMA domains showed higher dissipation than PBMA as seen from figure 11(b), which is consistent with the observation in [23]. As evident from figure 11(a), PLMA domains showed relatively lower contact stiffness compared to PBMA, which is expected as PLMA is rubbery at room temperature whereas PBMA is glassy. Unexpectedly, intermediate size PLMA domains show relatively higher stiffness. We speculate that the higher stiffness of the intermediate sized PLMA domains is due to sub-surface PBMA. We will investigate the reasons for the unexpected higher stiffness of intermediate sized PLMA domains by using the real-time module to estimate the stiffness for different levels of tip–sample interaction (different levels of tip–sample interaction can be achieved by altering the set-point amplitudes).

From these experiments, it is established that the developed module is able to provide real-time simultaneous estimates of stiffness and dissipation properties of the sample. We remark that the traditional images of height, phase and amplitude can be simultaneously obtained together (shown in figure B3 included in SI available at [stacks.iop.org/Nano/24/265706/mmedia](http://stacks.iop.org/Nano/24/265706/mmedia)) with the stiffness and dissipation images. Such a capability provides a rich source for researchers

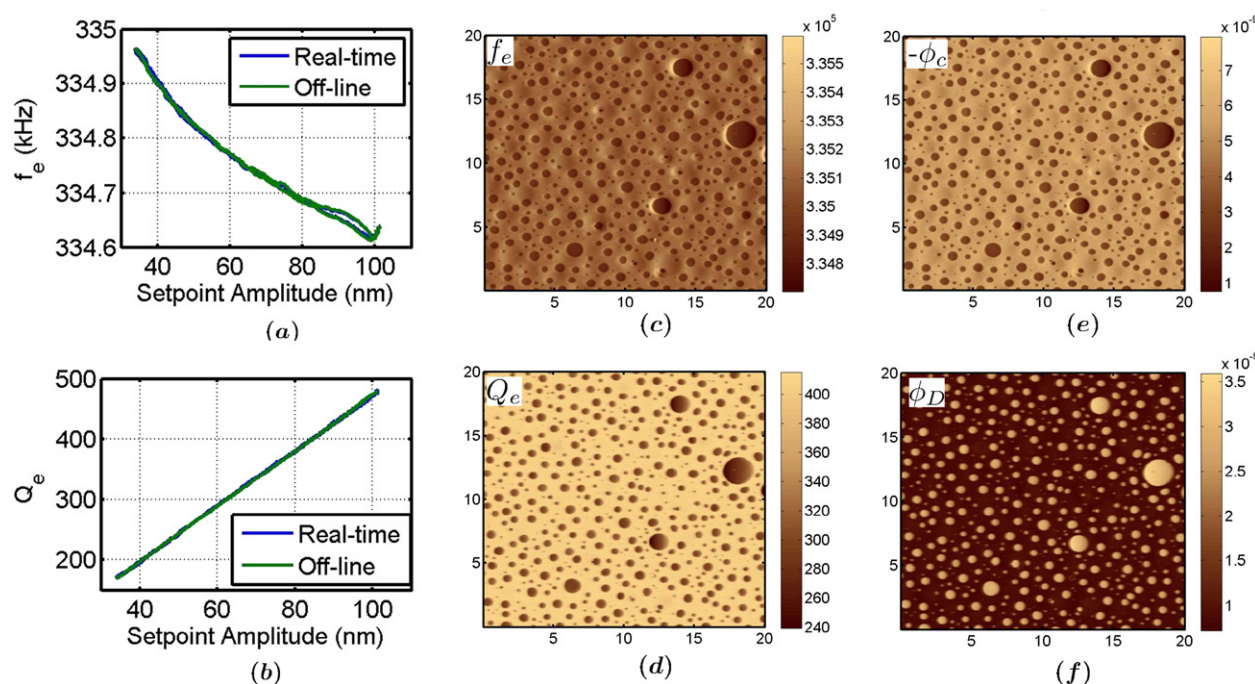


**Figure 10.** Figure shows (a) equivalent resonant frequency and (b) equivalent quality factor versus amplitude ‘approach–retract’ curve on PLMA polymer as calculated from Matlab (Off-line, green curve) and FPGA module (real-time, blue curve). Both curves match each other, verifying the estimates determined by real-time module. (c) and (d) shows  $20\ \mu\text{m} \times 20\ \mu\text{m}$  images of equivalent resonant frequency ( $f_e$ ) and equivalent quality factor ( $Q_e$ ) of PBMA/PLMA polymer blend respectively.  $f_e$ ,  $Q_e$  and amplitude image (shown in figure B3(b) included in SI available at [stacks.iop.org/Nano/24/265706/mmedia](http://stacks.iop.org/Nano/24/265706/mmedia)) were used to determine  $\Phi_c$  (in N) and  $\Phi_D$  (in Joules). They are depicted in figure (e) and (f) respectively.

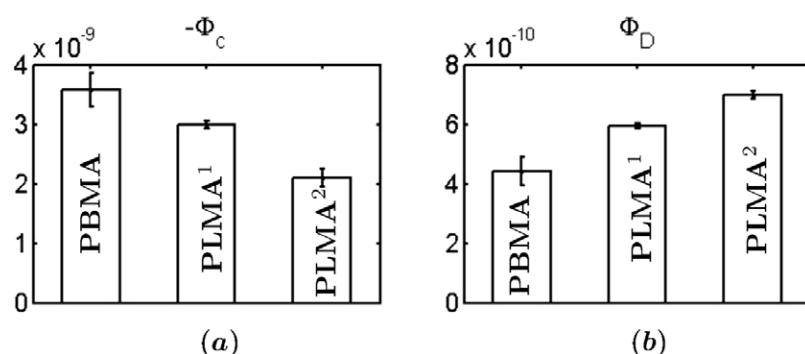


**Figure 11.** Figure shows mean (a)  $-\bar{\Phi}_c$  and (b)  $\bar{\Phi}_D$  of PBMA and PLMA polymers. The 1st data point is for PBMA domains and the 2nd and 3rd data points are for intermediate size and large size PLMA domains respectively. It is clear that both types of PLMA domains have lower stiffness and higher dissipation as compared to the smaller PBMA domains.

to interpret and discern material properties and to discern sources that lead to these properties.

## 7. Conclusion

Recent capabilities of controlling matter at the nanoscale have lead to new possibilities of achieving functionality of material with hitherto unparalleled specificity. Such a quest for designing material at the nanoscale has provided renewed urgency for real-time methods for determining material properties at the nanoscale. Probe based instruments have a spatial resolution that is well suited for nanoscale interrogation. However, currently there

is a lack of methods for soft-matter investigation with temporal resolution compatible with real-time needs. In this paper we report a method for simultaneously determining elasticity, dissipativity, and topography of material at the nanoscale in real-time in a dynamic mode operation of atomic force microscopy, which renders it suitable for soft-matter investigation. We demonstrate that averaging/perturbation analysis can be fruitfully employed to envision the possible complex system of a probe interacting with the sample as a linear and time-invariant (LTI) system with parameters that are governed by the dissipation and stiffness of the material. Such a model holds in a time scale smaller than that of the amplitude dynamics. Furthermore we have demonstrated

that a real-time adaptive estimation of the parameters of the model can be realized within the time-scale in which the LTI assumption holds. We have demonstrated the efficacy of the method, which is implemented on a FPGA based hardware module for imaging a polymer blend. The preliminary study of the polymer blend illustrates the new found capabilities for soft-matter research made possible by the methods developed here.

The equivalent LTI model and the time-scale of its validity might also allow for determination of material properties such as electrical and thermal properties. Moreover, recently, multiple modes of the cantilever flexure are being employed for nanoscale investigation. The paradigm developed in this paper along with the recent work on higher mode contributions [24] provides a framework for generalizing the methods developed here for such extensions and is a topic of future research.

## Acknowledgments

This research was supported by National Science Foundation under grant ECCS-1202411, awarded to Murli Salapaka and Greg Haugstad.

## Appendix. Proof of theorem 3.1

Equation (2) can be written as

$$\ddot{p} + \omega^2 p = \epsilon f(p, \dot{p}) + \epsilon E(t) \quad (\text{A.1})$$

where

$$f(p, \dot{p}) = \frac{-c\dot{p} + \phi(p, \dot{p})}{m}; \quad E(t) = g(t)/m. \quad (\text{A.2})$$

Change of coordinates, as in equation (3) gives

$$\begin{aligned} \dot{a} &= -\frac{\epsilon}{\gamma} [\Delta a \cos(\gamma t + \theta) + f(p, \dot{p}) + E(t)] \sin(\gamma t + \theta) \\ \dot{\theta} &= -\frac{\epsilon}{a\gamma} [\Delta a \cos(\gamma t + \theta) + f(p, \dot{p}) + E(t)] \cos(\gamma t + \theta). \end{aligned} \quad (\text{A.3})$$

Here  $f(p, \dot{p}) = f(a \cos(\gamma t + \theta), -a\gamma \sin(\gamma t + \theta))$  is periodic with period  $2\pi/\gamma$ . Equation (A.3) is exact, that is there are no approximations, and the vector field is the sum of finite periodic fields, that is:

$$\begin{pmatrix} \dot{a} \\ \dot{\theta} \end{pmatrix} = -\epsilon F(a, \theta, t) =: \begin{pmatrix} F_1(a, \theta, t) \\ F_2(a, \theta, t) \end{pmatrix} \quad (\text{A.4})$$

where  $F$  is sum of finite periodic vector fields. Thus averaging applies. Now,

$$\begin{aligned} g(t) \sin(\gamma t + \theta) &= [A \sin \gamma t + B_1 \sin(\gamma - \alpha)t \\ &\quad + B_2 \sin(\gamma + \alpha)t] \sin(\gamma t + \theta) \end{aligned}$$

which gives

$$\begin{aligned} g(t) \sin(\gamma t + \theta) &= \frac{\cos \theta}{2} [A + \cos \alpha t (B_1 + B_2)] \\ &\quad + \frac{\sin \theta \sin \alpha t}{2} (B_2 - B_1) \end{aligned}$$

$$\begin{aligned} &= -\frac{\cos(2\gamma t + \theta)}{2} [A + \cos \alpha t (B_1 + B_2)] \\ &\quad + \frac{\sin(2\gamma t + \theta) \sin \alpha t}{2} (B_2 - B_1) \\ &=: f_1(t, \alpha t, \theta). \end{aligned} \quad (\text{A.5})$$

Similarly,

$$\begin{aligned} g(t) \cos(\gamma t + \theta) &= -\frac{\sin \theta}{2} [A + \cos \alpha t (B_1 + B_2)] \\ &\quad + \frac{\cos \theta \sin \alpha t}{2} (B_2 - B_1) \\ &\quad + \frac{\sin(2\gamma t + \theta)}{2} [A + \cos \alpha t (B_1 + B_2)] \\ &\quad + \frac{\cos(2\gamma t + \theta) \cos \alpha t}{2} (B_2 - B_1) \\ &=: f_2(t, \alpha t, \theta). \end{aligned} \quad (\text{A.6})$$

This gives

$$\begin{aligned} F_1(a, \theta, t) &= \frac{1}{\gamma} [\Delta a \cos(\gamma t + \theta) + f(p, \dot{p})] \sin(\gamma t + \theta) \\ &\quad + \frac{1}{\gamma \epsilon} f_1(t, \alpha t, \theta) \\ F_2(a, \theta, t) &= \frac{1}{a\gamma} [\Delta a \cos(\gamma t + \theta) + f(p, \dot{p})] \cos(\gamma t + \theta) \\ &\quad + \frac{1}{a\gamma \epsilon} f_2(t, \alpha t, \theta). \end{aligned} \quad (\text{A.7})$$

So equation (A.4) can be written as

$$\begin{pmatrix} \dot{a} \\ \dot{\theta} \end{pmatrix} = -\epsilon F(a, \theta, t, \alpha t). \quad (\text{A.8})$$

Let us introduce the new independent variable  $\tau = \alpha t$ , then the system can be written as

$$\begin{pmatrix} \dot{a} \\ \dot{\theta} \end{pmatrix} = -\epsilon F(a, \theta, t, \tau) \quad (\text{A.9})$$

$$\dot{\tau} = \alpha$$

with appropriate initial conditions. As  $F$  is periodic over  $2\pi/\gamma$ , we can average the system over  $t$ , keeping  $\tau$  constant, which gives the averaged equations

$$\begin{pmatrix} \dot{a}_{av} \\ \dot{\theta}_{av} \end{pmatrix} = -\epsilon F^0(a_{av}, \theta_{av}, t, \tau_{av}) \quad (\text{A.10})$$

$$\dot{\tau}_{av} = \alpha$$

or

$$\begin{pmatrix} \dot{a}_{av} \\ \dot{\theta}_{av} \end{pmatrix} = -\epsilon F^0(a_{av}, \theta_{av}, t, \alpha t) \quad (\text{A.11})$$

where  $F^0() = (\gamma/2\pi) \int_0^{2\pi/\gamma} F() dt$ .

Then from [18], we have  $a_{av}(t) - a(t) = \mathcal{O}(\epsilon)$ , and  $\theta_{av}(t) - \theta(t) = \mathcal{O}(\epsilon)$  on the time scale  $1/\epsilon$ . After averaging  $F$  over the period  $2\pi/\gamma$ , and making the approximation



$2\gamma \approx \gamma + \omega$ , we finally get

$$\begin{aligned}\dot{a} &= -\frac{c_e(a)a}{2m} - \frac{1}{\gamma} \left[ \frac{\cos \theta}{2} (A + (B_1 + B_2) \cos \alpha t) \right. \\ &\quad \left. + \frac{\sin \theta \sin \alpha t}{2} (B_2 - B_1) \right] \\ \dot{\theta} &= \omega_e(a) - \omega + \frac{1}{a\gamma} \left[ \frac{\sin \theta}{2} (A + (B_1 + B_2) \cos \alpha t) \right. \\ &\quad \left. - \frac{\cos \theta \sin \alpha t}{2} (B_2 - B_1) \right]\end{aligned}\quad (\text{A.12})$$

where the equivalent damping coefficient  $c_e$  and resonant frequency  $\omega_e$  are again given by equation (6). The solution is equivalent to that of a linear system with damping coefficient  $c_e$  and resonant frequency  $\omega_e$  forced by a input of form  $g(t)$ , thus further bolstering the equivalent cantilever concept for multitone excitation.

## References

- [1] Binnig G, Quate C F and Gerber C 1986 Atomic force microscope *Phys. Rev. Lett.* **56** 930
- [2] Jesse S, Kalinin S V, Proksch R, Baddorf A P and Rodriguez B J 2007 The band excitation method in scanning probe microscopy for rapid mapping of energy dissipation on the nanoscale *Nanotechnology* **18** 435503
- [3] Gannepalli A, Yablon D G, Tsou A H and Proksch R 2011 Mapping nanoscale elasticity and dissipation using dual frequency contact resonance AFM *Nanotechnology* **22** 355705
- [4] Nikiforov M P, Jesse S, Morozovska A N, Eliseev E A, Germinario L T and Kalinin S V 2009 Probing the temperature dependence of the mechanical properties of polymers at the nanoscale with band excitation thermal scanning probe microscopy *Nanotechnology* **20** 395709
- [5] Balke N, Jesse S, Morozovska A N, Eliseev E, Chung D W, Kim Y, Adamczyk L, Garcia R E, Dudney N and Kalinin S V 2010 Nanoscale mapping of ion diffusion in a lithium-ion battery cathode *Nature Nanotechnol.* **5** 749–54
- [6] Kalinin S V, Rodriguez B J, Jesse S, Maksymovych P, Seal K, Nikiforov M, Baddorf A P, Kholkin A L and Proksch R 2008 Local bias-induced phase transitions *Mater. Today* **11** 16–27
- [7] Garcia R and Herruzo E T 2012 The emergence of multifrequency force microscopy *Nature Nanotechnol.* **7** 217–26
- [8] Haugstad G 2012 *Atomic Force Microscopy: Understanding Basic Modes and Advanced Applications* (New York: Wiley)
- [9] Martínez N F and García R 2006 Measuring phase shifts and energy dissipation with amplitude modulation atomic force microscopy *Nanotechnology* **17** S167
- [10] Melcher J, Carrasco C, Xu X, Carrascosa J L, Gómez-Herrero J, José de Pablo P and Raman A 2009 Origins of phase contrast in the atomic force microscope in liquids *Proc. Natl Acad. Sci.* **106** 13655
- [11] Gannepalli A, Sebastian A, Cleveland J and Salapaka M 2005 Thermally driven non-contact atomic force microscopy *Appl. Phys. Lett.* **87** 111901
- [12] Sebastian A and Salapaka S 2005 Design methodologies for robust nano-positioning *IEEE Trans. Control Syst. Technol.* **13** 868–76
- [13] Salapaka S, De T and Sebastian A 2005 Sample-profile estimate for fast atomic force microscopy *Appl. Phys. Lett.* **87** 053112
- [14] Sebastian A, Gannepalli A and Salapaka M V 2007 A review of the systems approach to the analysis of dynamic-mode atomic force microscopy *IEEE Trans. Control Syst. Technol.* **15** 952–9
- [15] Agarwal P and Salapaka M V 2009 Real time estimation of equivalent cantilever parameters in tapping mode atomic force microscopy *Appl. Phys. Lett.* **95** 083113
- [16] Paulo A S and Garcia R 2002 Unifying theory of tapping-mode atomic-force microscopy *Phys. Rev. B* **66** 041406(R)
- [17] Sebastian A, Salapaka M V, Chen D J and Cleveland J P 1999 Harmonic analysis based modeling of tapping-mode AFM *Proc. American Control Conf. (June)* pp 232–6
- [18] Sanders J A, Verhulst F and Murdock J A 2007 *Averaging Methods in Nonlinear Dynamical Systems* (Berlin: Springer)
- [19] Sebastian A, Salapaka M V, Chen D and Cleveland J P 2001 Harmonic and power balance tools for tapping-mode atomic force microscope *J. Appl. Phys.* **89** 6473–80
- [20] Bogoliubov N N and Mitropolskii Y A 1961 *Asymptotic Methods in the Theory of Non-Linear Oscillations* (New Delhi: Hindustan Publishing Corporation)
- [21] Ding F, Chen T and Qiu L 2006 Bias compensation based recursive least-squares identification algorithm for miso systems *IEEE Trans. Circuits Syst. II: Express Briefs* **53** 349–53
- [22] Cleveland J P, Anczykowski B, Schmid A E and Elings V B 1998 Energy dissipation in tapping-mode atomic force microscopy *Appl. Phys. Lett.* **72** 2613
- [23] Haugstad G and Wormuth K 2011 Digital pulsed force mode AFM and confocal Raman microscopy in drug-eluting coatings research *MRS Proc.* (Cambridge: Cambridge University Press)
- [24] Saraswat G and Salapaka M V 2013 On contribution and detection of higher eigenmodes during dynamic atomic force microscopy *Appl. Phys. Lett.* **102** 173108